Modelling thermodiffusive instabilities in hydrogen flames and their impact on the combustion process in a direct-injection hydrogen engine

Combustion and Flame 282 (2025) 114457

Contents lists available at ScienceDirect

Combustion and Flame

journal homepage: www.sciencedirect.com/journal/combustion-and-flame

Modelling thermodiffusive instabilities in hydrogen flames and their impact on the combustion process in a direct-injection hydrogen engine

Andrea Scalambro, Andrea Piano *, Federico Millo

Politecnico di Torino, corso Duca degli Abruzzi, 24, Torino, Italy

ARTICLE INFO

Keywords:
Hydrogen thermodiffusive flame instabilities
Hydrogen internal combustion engine
3D-CFD simulations
Combustion modelling

ABSTRACT

Hydrogen-fueled Internal Combustion Engines (H_2-ICEs) are typically operated with lean mixtures to minimize NOx emissions and reduce the risk of abnormal combustion events. Due to hydrogen's low Lewis number, premixed hydrogen-air flames in lean conditions exhibit strong thermodiffusive instabilities, which make the numerical simulation of the combustion process particularly challenging. Indeed, the intensity of these instabilities is significantly influenced by thermodynamic parameters – such as mixture temperature, pressure, and dilution rate – resulting in substantial variations in combustion behaviour across different operating conditions. Therefore, they have to be properly considered not only to ensure model robustness, but also to improve model accuracy over a wider range of operations. In this study, the combustion process in a Direct Injection H_2-ICE was analyzed using 3D-CFD simulations, relying on a flamelet-based combustion model. Two sets of lookup flame speed maps were defined: laminar flame speed (S_L) maps derived from standard 1D-CFD simulations in homogeneous reactor, and freely propagating flame speed (S_M) maps which account for the effects of thermodiffusive instabilities. The model that uses S_L maps required the recalibration of some combustion model parameters when changing the dilution rate to ensure consistency with experimental data. Instead, the model relying on S_M maps featured a noticeable accuracy across different air-to-fuel ratios without the need for recalibration any combustion model parameter, highlighting the key role of thermodiffusive flame instabilities on the combustion process. Based on these findings, the impact of such instabilities was evaluated throughout the entire combustion process from both global and local perspectives. The relevance of thermodiffusive instabilities was observed to increase with the air-to-fuel ratio, thereby enhancing combustion speed in leaner mixtures. Additionally, the implementation of thermodiffusive instabilities was found to affect also preferred direction of flame propagation, as stronger instabilities were identified in the leanest and low-temperature portions of the flame front.

Novelty and significance

This study addresses a critical knowledge gap regarding the role of thermodiffusive flame instabilities in accurately replicating the combustion process of a direct-injection internal combustion engine within a RANS simulation framework. Indeed, while these instabilities have been shown to significantly enhance the mixture consumption rate in quiescent environments at low to moderate pressures and temperatures, particularly in lean mixtures, their impact on the burn rate under engine-like conditions has not yet been systematically investigated, to the best of the authors' knowledge. This work provides a comprehensive analysis of the significance of these instabilities in the combustion process of a direct-injection hydrogen internal combustion engine. The analysis is conducted from both a global perspective, assessing their overall influence on the combustion process, and a local perspective, examining how they alter flame front characteristics when incorporated into the model.

1. Introduction

In spite of the massive shift toward electric vehicles [1], internal combustion engines (ICEs) will continue to play a pivotal role in the transportation sector over the next decades [2,3]. To comply with the increasingly stringent emissions regulations aimed at reducing the environmental impact of the sector, in recent years, new generations of engines have been developed with higher efficiency and lower emissions [4]. In this context, low carbon and carbon-free fuels are increasing their strategic relevance [5,6], as they would allow the partial or complete

* Corresponding author.
E-mail address: andrea.piano@polito.it (A. Piano).

https://doi.org/10.1016/j.combustflame.2025.114457
Received 18 March 2025; Received in revised form 1 September 2025; Accepted 2 September 2025
Available online 17 September 2025

elimination of emissions of fossil carbon dioxide (CO_2) into the atmosphere [7]. In this regard, certain alcohols, such as methanol [8–10] and ethanol [11,12], biodiesel [13,14], ammonia [15–17], and hydrogen [18] have already demonstrated their effectiveness as alternatives in combustion engines in place of fossil fuels. Among these, hydrogen is particularly promising thanks to its high energy density and the potential for clean production through multiple renewable pathways. While its large-scale availability and long-distance transportability remain under development, ongoing efforts worldwide are steadily addressing these challenges. This makes hydrogen a standout candidate for replacing fossil fuels in internal combustion applications [18], especially for high-energy-demand and high-load operations, hence including heavy-duty and off-road machinery. The viability of hydrogen as a fuel for internal combustion engines is further supported by the current development of prototype vehicles equipped with hydrogen engines by numerous manufacturers [19]. Compared to conventional fossil fuels, such as gasoline, hydrogen exhibits several physical, chemical, and thermodynamic properties that make it highly suitable for use as a fuel in ICEs, while also presenting certain challenges in practical applications [20]. Indeed, the wide flammability limits (from 4 % to 75 % volume in air) allow ultra-lean operations, potentially zeroing nitrogen oxides (NOx) emissions [21]. Moreover, the high laminar flame speed [22], even under extremely lean conditions, reduces combustion duration, increasing thermal efficiency. Additionally, its high knock resistance [23] allows the exploitation of higher compression ratios, resulting in higher efficiency. However, the high adiabatic flame temperature and the low quenching distance might increase wall heat losses and increasing the risk of backfiring in case of external mixture preparation, as the flame can easily passes through an almost closed valve [24]. This issue can be further compounded by the lower ignition energy of hydrogen (more than one order of magnitude lower than gasoline, diesel and methane at 1 bar and in a stoichiometric mixture) [25,26], which can also promote the onset of uncontrolled combustion processes (e.g., pre-ignition). Lastly, the combination between the low ignition energy and the small quenching distance contributes to the onset of knock at higher engine speeds, if compared to gasoline engines [27]. Therefore, the engine design and its optimization require a deep understanding of the complex phenomena that govern the combustion process. In this framework, multi-dimensional numerical simulations serve as an effective tool to analyze and predict combustion dynamics, and optimize engine performance under various operating conditions [28]. Some numerical studies on pre-ignition [29], knock [30,31], and backfiring [32,33] are already present in the literature. However, these phenomena are highly dependent on the previous injection and combustion processes, making it essential to develop computational methodologies that enhance the predictive accuracy of the models. Focusing on combustion, both models based on the flamelet assumption, such as the Extended Coherent Flamelet Model (ECFM) [34] or the G-equation combustion model [35], and based on the Well-Stirred Reactor (WSR), i.e. on detailed chemistry, such as the SAGE [36], have been already adopted. In [36] the combustion process of a port fuel injection (PFI) H_2-ICE was investigated using detailed chemistry coupled with preferential species diffusion to account for the higher hydrogen diffusivity. Model outcomes were compared to experiments across different engine loads and operating relative air-to-fuel ratios (λ), demonstrating good agreement with the experimental results, although with a slight tendency towards faster burn rates. In [37], the same combustion model was exploited to predict knock occurrence for different operating λ in a spark-ignition (SI) H_2-ICE. Additionally, the model was adopted to perform a preliminary assessment of NOx emissions. In [38], the detailed chemistry combustion model was used to assess the impact of λ in a direct injection (DI) H_2-ICE on combustion efficiency and compared against PFI cases, modelled assuming perfectly premixed charge in the intake system. A very high combustion efficiency was found at $\lambda = 2.0$ and $\lambda = 3.0$ for the PFI cases, while it significantly drops at $\lambda = 3.5$. In DI operation, the injection timing has instead a not negligible impact on combustion efficiency and duration since it affects the hydrogen-air mixing process. Similarly, in [35] a 3D numerical model of a DI H_2-ICE was developed and used to study the influence of the injection timing on the mixture formation process and combustion performance. Nevertheless, differently from the three works previously mentioned (i.e., [36–38]) in [35] Fu et al. adopted the G-equation combustion model, based on the flamelet assumption, and calibrated the laminar flame speed model for hydrogen to improve model accuracy. Also Sfrisoet al. in [39] used the G-equation model to simulate combustion in a PFI optically accessible engine under a wide range of operating conditions. In this case, laminar and turbulent flame speeds were calculated through Verhelst [40] and Zimmont [41] correlations, respectively. The agreement with experiments is notable, especially considering that no case-to-case calibration was performed. Nevertheless, as suggested by the authors, model accuracy could be further improved through the implementation of thermodiffusive instability effects on the tabulated flame speed maps used in the 3D computational fluid dynamics (CFD) model. A similar conclusion was reached by Maio et al. in [42]. In [42] the authors developed a 3D-CFD model based on the ECFM to describe the most relevant phenomena occurring in H_2-ICEs, with the objective of supporting the experimental data analysis. The model was then used to compare the performance of a PFI concept with that of a DI system and to predict knocking tendencies and NOx emissions under different operating conditions. However, in order to achieve a satisfactory agreement between the outcomes of the numerical model and the experiments, a recalibration of one of the combustion parameters (i.e., the turbulent stretch, see Section 3.1 for more details) was required. Also in this case the authors attribute this behaviour to the peculiarity of hydrogen flames in lean environments, which are characterized by strong thermodiffusive instabilities induced by the non-unity Lewis number of hydrogen. A first attempt to implement the effects of thermodiffusive instabilities in a 3D-CFD combustion model was proposed in [43]. Two different approaches were tested to compute laminar flame speed maps. On one hand, 1D-CFD simulations were conducted in a homogeneous reactor based on the reaction mechanism proposed by Kéromnès et al. [44], and the analytical correlation proposed by Pessina et al. [45]. On the other hand, thermodiffusive instabilities were accounted for by applying a corrective factor following the correlation proposed by Berger in [46]. Both the approaches provided satisfactory results at relatively lean conditions (i.e., $\lambda = 2.4$), but only the tabulated approach led to reliable results at higher dilution rates (i.e., $\lambda = 3.0$). Hernandez et al. [47] further delve into the modelling of thermodiffusive flame instabilities occurring in hydrogen-air flames. To this purpose, the authors developed freely propagating flame speed (S_M) maps modifying standard laminar flame speed maps (S_L), derived from 1D-CFD simulations relying on the Konnov mechanism [48], by using the scaling methodology based on direct numerical simulations (DNS) proposed by Howarth et al. [49]. Three λ values were tested (i.e., $\lambda = 2.5$, $\lambda = 3.0$, and $\lambda = 3.5$) and results obtained with the modified flame speed maps (i.e., freely propagating flame speed) displayed better agreement with experimental data across all the tested λ values, compared to the standard laminar flame speed maps. Nevertheless, the extent of the correction introduced by the modified flame speed maps was not clearly assessed. In light of the reported findings, it appears clear the need of utilizing flame speed maps which include the effects of thermodiffusive flame instability to properly replicate the combustion process of H_2-ICE in 3D-CFD frameworks which rely on combustion models based on the flamelet assumption. Nevertheless, despite the extensive body of fundamental studies on thermodiffusive instabilities available in the literature, primarily based on DNS [50,51], the effect of their implementation into simplified yet comprehensive 3D-CFD environments using Reynolds-averaged Navier-Stokes (RANS) models has yet to be addressed in a systematic way and it remains not entirely understood. In this context, the scope of the present work can be summarized as follows. The first objective is the development of a 3D-CFD RANS model capable of replicating in-cylinder phenomena in a DI H_2-ICE, including

gas exchange, hydrogen injection, hydrogen-air mixing, and combustion processes. The second objective focuses on evaluating the impact of incorporating thermodiffusive flame instabilities in the 3D-CFD model from both a global perspective (e.g., reaction rates) and a local perspective (e.g., flame morphology) across various dilution rates. Experimental tests to calibrate and validate the numerical model were carried out at FEV facilities in Aachen on a Rehlko (formerly Kohler Energy) prototype DI H_2-ICE for off-road applications.

The paper is structured as follows. First, a brief overview of the test case and the operating conditions selected for the analysis is provided. Then, the main features of the 3D-CFD model used for the numerical analysis are presented, with particular emphasis on the combustion model. Next, the numerical procedure for the evaluation of flame speed maps, which account for the effects of thermodiffusive instabilities on the reaction rate, is described in detail. The outcomes of this procedure, which combines 0D and 1D-CFD calculations, are then analyzed to assess the impact of thermodiffusive flame instabilities under varying thermo-chemical conditions. This is followed by a brief examination of the injection and mixing processes, which define the boundary conditions for combustion simulations. Finally, the key findings of this research are discussed, with a particular focus on the impact of thermodiffusive instabilities on the combustion process from both global and local perspectives.

2. Test case

Experimental tests and numerical simulations were carried out on the 4-cylinders, 2.48-liter Rehlko KDH DI H_2-ICE, whose main features are reported in Table 1. The engine was retrofitted from a state-of-the art diesel engine for off-road applications, implementing only minimal and compulsory modifications to drastically reduce conversion costs. Therefore, the geometry of the intake ports, which induce a strong swirl motion and the flat flamedeck of the diesel engine were retained on the H_2-ICE. Conversely, the compression ratio (CR) was decreased to 11:1, by replacing the omega-shaped diesel piston bowl with a wider, deeper and flat bowl design, aimed at mitigating the risk of knock. Additionally, the engine was equipped with a turbocharging system featuring a variable nozzle turbine (VNT) properly dimensioned for lean hydrogen operations. A low-pressure (LP) hydrogen injector, characterized by a maximum injection pressure of 25 bar, was mounted laterally, close to the glow plug of the original diesel engine. Despite the extremely limited number of design adaptations, the H_2-ICE achieved the same performance of the diesel one.

Several sweeps of the main calibration parameters in terms of dilution level, injection timing, and combustion anchor angle (MFB50) were carried out at the dynamic test bench. In the present study the working point (WP) 1000 rpm – 200 Nm (11 bar of IMEP) was selected for the analysis considering three λ levels (i.e., 1.8, 2.0, 2.3) with almost constant end of injection (EOI), and MFB50, thus allowing the effects related to the implementation of thermodiffusive instabilities in the 3D-CFD model to be linked solely to the dilution level of the mixture.

Table 1
Kohler KDH engine specifications.

N° of Cylinders	4 In-line
Displacement [cm^3]	2480
Bore x Stroke	88 mm x 102 mm
Stroke/Bore	1.16
Compression Ratio	11:1
N° of valves	16
Turbocharging	VNT
Fuel Injection	Direct Injection (up to 25 bar)
Intake Ports Design	High-Swirl
Rated Power [kW]	55 kW @ 2600 RPM
Rated Torque [Nm]	315 Nm @ 1600 RPM

3. Numerical framework

3.1. 3D-CFD simulation setup

Multidimensional numerical simulations were performed by means of the commercially available software Converge CFD v3.1.9 using a RANS approach. In this framework, the RNG $k-\varepsilon$ turbulence model was adopted to close the Reynolds stress tensor. In the simulation of in-cylinder phenomena of DI H_2-ICE, the proper modeling of turbulence is of paramount importance to accurately describe the hydrogen-air mixing process. As reported in [52,53], all the $k-\varepsilon$ turbulence models (i.e., standard $k-\varepsilon$, realizable $k-\varepsilon$, and RNG $k-\varepsilon$) lead to a good agreement with optical data and minimal differences arise from the use of one or another of them. Nevertheless, the RNG $k-\varepsilon$ model was here adopted, as it is better captures the evolution of rotating vortices, such as the strong swirl, characteristic of the present case study [54]. Time-varying boundary conditions, in terms of temperature and pressure, were imposed on the inflow and outflow section of the computational domain. They were derived from a 1D-CFD complete engine model developed in GT-SUITE v2023, correlated against experimental data gathered at the dynamic test bench. Additionally, the GT-SUITE model was adopted to define species concentration within the computational domain at the start of the simulation. Simulations were initiated during the exhaust stroke (i.e., 270 CAD aTDCf) to ensure a properly initialized fluid volume, with particular attention to the flow field, at the beginning of the intake stroke. The computational domain was discretized through an orthogonal mesh with a base dimension equal to 4.00 mm. The Adaptive Mesh Refinement (AMR) algorithm was adopted to automatically refine the mesh up to 0.25 mm, based on velocity, temperature, and hydrogen concentration sub-grid scale (SGS). Additionally, fixed mesh refinements (0.50 mm) were added to all the boundaries of the combustion chamber to better describe the interaction between the hydrogen jet and the cylinder walls. Lastly, a minimum grid size of 62.5 μm mm was reached in the spark plug gap to improve the modeling accuracy of the first flame kernel. The simulation time step was controlled using a variable time-step algorithm. Specifically, the time step was limited by three Courant Friedrich Lewy (CFL) numbers, i.e., $CFL_{Convection} = 1.0$, $CFL_{Diffusion} = 2.0$, and $CFL_{Mach} = 50.0$. As a results, the timestep was approximately between 1.5 μs and 60 ns (during injection). Lastly, the temperature of the walls was imposed based on the outcomes of the 1D-CFD model, and the wall-function from O'Rourke and Amsden [55] was used to model the wall turbulent heat transfer. Injection was simulated by including the actual injector geometry within the computational domain. Only the bottom part of the injector, made up of the injector valve and the injector guiding cap, was considered in the analysis as the turbulence produced inside the injector volume is almost negligible compared to those induced by the guiding cap [42]. This approach guaranteed a significant reduction in computational cost. Hydrogen mass flow rate was hence imposed on a section located few millimetres upstream of the injector valve (normal gradient as pressure boundary condition) and the actual motion of the injector pintle was provided as a simulation input. The temperature of the injected hydrogen was kept equal to 60 °C for all the analyzed WPs. The described injection model has been previously validated against experimental data gathered from an optically accessible constant volume chamber under various ambient and injection pressures, and injection durations [56].

3.1.1. Combustion modelling

Combustion was modeled using the ECFM, a combustion model derived from the Coherent Flame Model (CFM) [57], and specifically developed to describe premixed combustion processes [58] evolving in the flamelet region. It relies on tabulated flame speed maps derived either from one-dimensional calculations or from analytical

correlations. Therefore, compared to chemistry-based combustion models, which are based on the WSR hypothesis, computational costs are significantly reduced, as detailed chemistry calculations are avoided. Compared to the CFM, the ECFM incorporates a conditional averaging technique that more accurately defines the composition and state of the fresh gases entrained by the flame, thereby enhancing the evaluation of the local laminar flame speed. This makes this combustion model particularly suitable for the simulation of stratified mixtures, that generally characterize DI spark ignition (SI) engines. The ECFM relies on the assumption that the oxidation of the fuel occurs in an extremely thin layer that splits the fresh mixture by the burned gases and propagates toward the unburned gases. The mean reaction rate $\dot{\omega}$ is given by the product between the flame surface density Σ (i.e., the flame surface area per unit volume, representative of the flame front convolutions), the Reynolds averaged density in the fresh gases $\overline{\rho_u}$ and the unstretched laminar flame speed S_L (Eq. (1)).

$$\dot{\omega} = \overline{\rho_u} S_L \Sigma \tag{1}$$

This approach allows decoupling chemistry features, incorporated into the average flame speed, from turbulent interactions, which are instead included in the flame surface density. The flame surface density is determined by the following transport equation (Eq. (2)) [59,60]:

$$\frac{\partial \Sigma}{\partial t} + \frac{\partial u_i \Sigma}{\partial x_i} = \frac{\partial}{\partial x_i}\left(\frac{\mu}{Sc}\frac{\partial \Sigma/\overline{\rho}}{\partial x_i}\right) + (P_1 + P_2 + P_3)\Sigma - D + P_k \tag{2}$$

Where μ is the molecular viscosity, Sc is the Schmidt number, and u_i is the Favre averaged mean velocity component. P_1 (Eq. (3)), P_2 (Eq. (4)), and P_3 (Eq. (5)) are respectively the flame surface production by turbulent stretch, the production term by the mean flow dilatation, and the consumption due to flame thermal expansion and curvature.

$$P_1 = \alpha K_t \tag{3}$$

$$P_2 = \frac{2}{3}\frac{\partial u_i}{\partial x_i} \tag{4}$$

$$P_3 = \frac{2}{3}\frac{\rho_u}{\rho_b} S_L \frac{1 - \widetilde{c_\Sigma}}{\widetilde{c_\Sigma}} \Sigma \tag{5}$$

In the term P_1 (Eq. (3)), α is a calibration constant named turbulent stretch parameter, while the turbulent stretch (K_t) depends on the Intermittent Turbulent Net Flame Stretch (ITNFS) model [61]. Specifically, the ITNFS model allows to take into account the effects of a complete turbulent flow field, characterized by a wide range of scales, on the propagation of the flame front. In the ITNFS model, K_t is given as

$$K_t = \frac{k}{\varepsilon} ITNFS_{factor} \Gamma_k \left(\frac{u'}{S_L}, \frac{L}{\delta_l}\right) \tag{6}$$

Where ε is the turbulent dissipation, k is the turbulent kinetic energy, $u' = \sqrt{2k/3}$ is the turbulence RMS velocity and δ_l is the laminar flame thickness computed as described in [62] and Γ_k is the net stretch ratio function. The stretch ratio function is evaluated as an integration of the efficiency function (C), whose complete formulation is provided in [61]. $\widetilde{c_\Sigma}$ is the flame surface density progress variable. In Eq. (2), D is the destruction due to consumption, which is function of the constant for the surface density destruction term β, S_L, Σ, and the volume progress variable $\bar{c}$ (Eq. (7)).

$$D = \beta S_L \frac{\Sigma^2}{1 - \bar{c}} \tag{7}$$

Lastly, P_k (Eq. (2)) is the source term, used to account for external energy sources, as the one released by the spark plug.

In the present activity, tabulated laminar flame speed maps were computed through the one-dimensional laminar premixed chemistry tool of Converge 3.1, using the combustion mechanism proposed by Zhang et al. [63], which includes 44 species and 251 reactions, and validated against experiments including ignition delay time data, species and temperature profiles versus time and flame speed measurements. Mono-dimensional simulations were performed for different levels of temperature (T_{min} = 500 K, T_{max} = 1500 K), pressure (p_{min} = 10 bar, p_{max} = 100 bar), Φ (Φ_{min} = 0.1, Φ_{max} = 1.0), and residual concentration (EGR) (EGR_{min} = 0, EGR_{max} = 0.15), with the aim of representing the entire set of thermo-chemical conditions encountered by the flame during the combustion process. Overall, 15,960 combinations were tested. To account for thermodiffusive flame instabilities, the tabulated flame speed maps were adjusted based on the theoretical framework developed by Howarth et al. [64] for laminar flows, as detailed in Section 3.2. Specifically, flame speed maps accounting for thermodiffusive flame instabilities (i.e., freely propagating flame speed) were adopted for the calculation of the reaction rate ($\dot{\omega}$), as well as for the production (P_3) and destruction (D) terms. The laminar flame thickness was not externally imposed but rather computed using the formulation proposed by Blint et al. [62], which expresses it as a function of the laminar flame speed. Consequently, by modifying the flame speed maps to include thermodiffusive effects, the flame thickness is indirectly influenced as well. Although this approach (i.e., the direct replacement of standard laminar flame speed maps with freely propagating ones) represents a significant assumption, the analysis was deliberately constrained to moderate values of λ (λ_{max} = 2.3) and low engine speeds, thereby limiting the Karlovitz (Ka) number to the corrugated and wrinkled flamelet regimes of turbulent combustion ($Ka \leq 1$). For high Ka numbers, alternative modeling approaches that explicitly incorporate turbulence chemistry interactions would be necessary. Indeed, at elevated Ka, turbulence and thermodiffusive effects exhibit synergistic and positive interactions, leading to increased flame stretch and, consequently, enhanced turbulent flame speeds [65].

3.2. Thermodiffusive flame instabilities

3.2.1. Theoretical background

Compared to conventional fossil fuels, hydrogen-air flames are characterized by significantly higher flame speeds [23,66,67]. This is mainly rooted in the following three causes: the lower hydrogen activation energy that increases the unstretched laminar burning velocities [68], the positive dependence of hydrogen flames on flame stretch (due to the negative Markstein number) [69], and the thermodiffusive instabilities [70]. Thermodiffusive instabilities arise from two coupled phenomena: differential diffusion and preferential diffusion. Differential diffusion results from the low Lewis number of hydrogen ($Le_{H_2} \approx 0.3$) [71] which induces an imbalance between species diffusion and thermal energy flux. In positively curved flame regions, the chemical energy of the fresh mixture enters the flame faster than the rate at which thermal energy is conveyed toward the preheat region, thus enhancing combustion speed. Conversely, in negatively curved regions, the opposite occurs. Simultaneously, preferential diffusion is driven by the difference in Lewis numbers between hydrogen and other oxidizing species ($Le_{O_2} \approx 1.0$). Preferential diffusion results in local enrichment of the flame in positively curved regions, which increases flame adiabatic temperature and consumption rate, further promoting the instability [72]. Hydrogen flames subjected to thermodiffusive instabilities are characterized by bulb-like structures [73], including both small-scale cellular structures and large-scale structures [74], that wrinkles the flame front even under laminar conditions. The magnitude of thermodiffusive flame instabilities has been assessed both through experiments [75,76] and, more recently, through high fidelity direct numerical simulations (DNS) [46,73,77–79] under laminar conditions. The findings from these studies provide strong evidence that lean hydrogen flames are prone to developing instabilities in conditions relevant to multiple combustion systems [80]. Also the interaction between flame instabilities and turbulence has been investigated through numerical experiments [81]. It resulted that flame acceleration is mainly governed

by local flame instabilities in the wrinkled flamelet regime and by turbulence intensity in the corrugated flamelet regime. Instead, in the corrugated flamelet regime, both mechanisms play a role in influencing flame propagation [82]. Additionally, the freely propagating flame speed values have proven to be more suitable for characterizing turbulent flames rather than the laminar ones [64]. Matalon et al. [49,71,83] showed that thermodiffusive instabilities in lean premixed hydrogen flames can be effectively characterized by the instability parameter ω_2, derived from classical stability analysis and reported in Eq. (8).

$$\omega_2 = -\left[B_1 + \beta\left(Le_{eff} - 1\right)B_2 + PrB_3\right] \tag{8}$$

If ω_2 takes positive values, the flame is unstable, meaning its propagation speed is enhanced by thermodiffusive instabilities. On the opposite, for $\omega_2 \leq 0$, the flame remains stable, and thermodiffusive instabilities do not increase the rate of propagation of the flame front. In Eq. (8), Pr is the Prandtl number, B_i are parameters which mainly depend on the temperature, on the density ratio (σ), and on the thermal conductivity (λ), and β is the Zeldovich number of the reaction, computed as shown in Eq. (9).

$$\beta = \frac{E_a(T_b - T_u)}{RT_b^2} \tag{9}$$

T_b and T_u are the adiabatic and unburned temperature respectively, R is the ideal gas constant and E_a is the overall activation energy using the approach of Law and Sung [68] (Eq. (10))

$$E_a = -2R\frac{d(\log f_0)}{d(1/T_b)} \tag{10}$$

Where f_0 is the laminar mass burning flux computed as the product between the density of the unburned gases and the laminar flame speed ($f_0 = \rho_u S_L$). Lastly, the Lewis effective number Le_{eff} used in Eq. (8) is computed exploiting the formulation proposed in [71] (Eq. (11)).

$$Le_{eff} = \begin{cases} \dfrac{Le_O + ALe_F}{1+A}, \; A = 1 + \beta\left(\Phi^{-1} - 1\right) \; if \; \Phi < 1 \\ \dfrac{Le_F + ALe_O}{1+A}, \; A = 1 + \beta(\Phi - 1) \; if \; \Phi > 1 \end{cases} \tag{11}$$

Le_O and Le_F are the oxidizer and fuel Lewis number respectively, and Φ is the global equivalence ratio. This approach allows the evaluation of ω_2 solely through inexpensive 0D/1D calculations. Berger et al. [84] and Howarth et al. [64,85] proposed empirical correlations to derive the freely propagating flame speed S_M from the laminar flame speed S_L and ω_2. Compared to the theory proposed by Berger, the validity range of Howarth's theory is larger, covering pressures up to 40 bar and equivalence ratios ranging from 0.565 to 0.2 ($1.75 < \lambda < 5.0$). Howarth's correlation is shown in Eq. (12).

$$\frac{S_M}{S_L} = \begin{cases} \exp(0.057\omega_2) \; if \; \Pi \leq \Pi_C \\ 1 + 0.22\omega_2 \; otherwise \end{cases} \tag{12}$$

Π_c is a normalized critical pressure that divides the low-pressure ($\Pi < \Pi_c$) from the high-pressure ($\Pi > \Pi_c$) regions ($\Pi = p\,/p_{ref}$, with $p_{ref} = 1\ atm$). Its formulation is reported in Eq. (13).

$$\Pi_C = \left(\frac{20\Phi}{7 - 2\Theta}\right)^{\frac{150}{21+10\Theta}} \tag{13}$$

Where $\Theta = T/T_{ref}$, with $T_{ref} = 300\ K$.

3.2.2. Instability parameter (ω_2) and freely propagating flame speed (S_M) evaluation

The evaluation of S_M maps requires ω_2 to be defined for each specific thermo-chemical condition used in the evaluation of S_L. To this purpose, chemistry-related data (i.e., Le_{eff} and Pr) needed for the evaluation of ω_2 were computed through the open-source code Cantera and coupled with combustion-related data (i.e., T_b, T_u, ρ_b, ρ_u, σ, E_a, and β) gathered by means of the 1D premixed chemistry tool of Converge, the same tool used for the evaluation of the S_L maps. In Fig. 1 the contour of the ω_2 parameter is reported as a function of pressure and Φ at a temperature of 700 K. For almost stoichiometric mixtures ($\Phi > 0.7$) and relatively low pressure ($p < 20\ bar$) the flame is stable, as ω_2 is equal to zero, and therefore S_M tends to be equal to S_L. For reducing Φ and/or increasing pressure the flame becomes unstable, as pointed out by the higher values reached by ω_2, until a bridge is met. After it, for even lower Φ or higher pressure, the flame evolves in the high-pressure ($\Pi > \Pi_c$) regime and the magnitude of ω_2 decreases again, but the flame remains unstable.

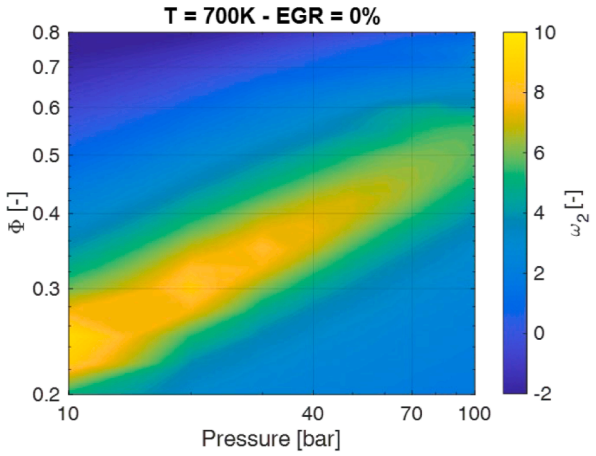

Fig. 1. Instability parameter ω_2 at 700 K as a function of pressure and Φ.

Moreover, ω_2 has shown high sensitivity to the temperature [49,80], displaying higher values at low temperatures and featuring larger unstable regions on the pressure-Φ map. For instance, at 300 K and ambient pressure (1 atm) the stable flame region is constrained for $\Phi > 0.6$, while at 700 K it expands up to $\Phi = 0.4$. The range of pressure and equivalence ratio and the temperature level reported in Fig. 1 have been chosen to allow a direct comparison with the ω_2 map reported in [64], which was derived from DNS. Nonetheless, compared to the latter, a narrow pressure interval has been shown in the present work, since the low-pressure region (from 1 to 10 atm) are not representative of engine-like conditions. Overall, a high level of agreement is obtained between the results reported in Fig. 1 and those shown in [64], both in terms of distribution and absolute values.

4. Results

4.1. Injection and mixing

Injection and mixing processes play a crucial role in determining combustion characteristics in DI H_2-ICEs as they directly influence turbulence levels, in-cylinder dynamics, and hydrogen distribution. Indeed, the injection event generates a significant increase in the turbulence kinetic energy within the cylinder, and the interaction between the high-speed hydrogen jet and the boundaries of the combustion chamber – especially the piston – alters the main aerodynamic structures inside the cylinder. Lastly, even though hydrogen is characterized by high diffusivity compared to other gaseous fuels, its distribution in the combustion chamber at spark timing (ST) is generally not perfectly homogeneous, especially for combustion systems not specifically designed for hydrogen

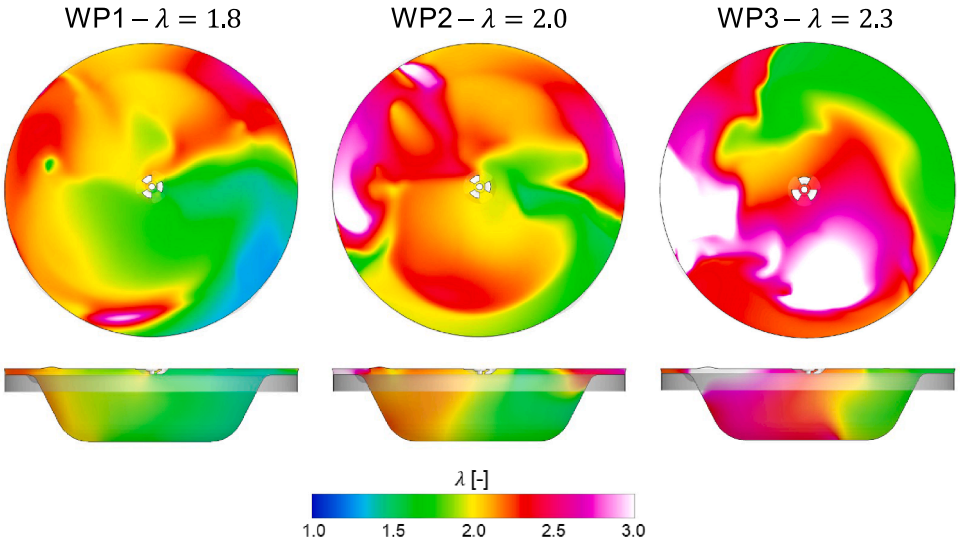

Fig. 2. Relative air-to-fuel ratio distribution at spark timing.

operation. Therefore, because of the high sensitivity of flame speed to the local λ, the hydrogen-air mixing process is strictly linked to the combustion evolution.

Fig. 2 displays λ distribution at ST on two planes: one of them is perpendicular to the cylinder axis (left), while the other one is orthogonal to the flame deck. Both planes pass through the spark plug gap. At $\lambda = 1.8$ there are no bulk regions characterized by a relative air-to-fuel ratio lower than 1.5 or higher than 3 and the local λ in between the spark plug gap is equal to the average λ (i.e., $\lambda = 1.8$). Then, as the dilution level of the mixture is increased, the richest portions of the mixture gradually decrease, and the leanest volumes progressively increase. The most interesting aspect is related to the spatial location of hydrogen within the combustion chamber. As a matter of fact, because of the similar injection timing, the interaction between the hydrogen jet and the piston is reasonably comparable among the different dilution levels. This induces a similar hydrogen distribution in the combustion chamber. Indeed, for all the WPs analyzed, the regions characterized by low λ values are located close to the liner, in correspondence of the intake valve opposite to the hydrogen injector. Additionally, a rich extension detaches from it and moves toward the spark plug. On the contrary, the regions characterized by low λ values are positioned below the intake and exhaust valve on the injector side.

4.2. Combustion

The combustion model was calibrated following the matrix reported in Table 2, and acting solely on the turbulent stretch parameter α (see Eq. (3)). In the first three calibration approaches (Cal. 1, Cal. 2, and Cal. 3), S_L maps (i.e., without including the effects of thermodiffusive instabilities) were adopted, while S_M maps (i.e., including the effects of thermodiffusive instabilities) were exploited in the fourth calibration attempt (Cal. 4). Cal. 1, Cal. 2, and Cal. 3 were calibrated respectively in the WP at $\lambda = 1.8$, $\lambda = 2.0$, and $\lambda = 2.3$, while Cal. 4 only at $\lambda = 2.3$. Since all the tested operating conditions are characterized by λ values significantly higher than 1.0 (lean mixture), the value assumed by ω_2 is on average always positive, leading to higher S_M if compared to S_L. Therefore, in Cal. 4 α is lower than the turbulent stretch values used for the cases which do not take into account thermodiffusive instabilities in the flame speed evaluation.

Table 2
Combustion model calibration matrix.

Reference Name	Calibration WP	Turbulent Stretch (α) [-]	Flame Instabilities
Cal. 1	$\lambda = 1.8$	0.90	No
Cal. 2	$\lambda = 2.0$	0.80	No
Cal. 3	$\lambda = 2.3$	1.00	No
Cal. 4	$\lambda = 2.3$	0.72	Yes

As shown in Fig. 3, where the grey area represents the envelope of the pressure and heat release rate traces of 800 consecutive engine cycles and the black line the experimental average, an adequate accuracy of the models which rely on S_L maps is obtained solely through the recalibration of α when the dilution rate changes. Instead, the model based on S_M maps features a more than satisfactory agreement with the experimental data across the entire λ sweep, without the need to change α. This result is particularly significant as it underscores the enhanced predictive capabilities of the model when thermodiffusive effects are taken into account.

To further evaluate the predictive capability of the developed model, which accounts for the effects of thermodiffusive flame instabilities, a ST sweep was conducted under the same conditions previously analyzed. For each of the three dilution rates, four additional STs were tested. For each of the 15 operating conditions, the same approach as in Calibration 4 was applied, accounting for thermodiffusive instabilities and setting the turbulent stretch parameter α to 0.72. The results, presented in terms of pressure and heat release rate (HRR), are shown in Fig. 4.

The fourth row corresponds to the operating conditions used for model calibration. In the first three rows, the ST is progressively advanced until an MFB50 of approximately 6 CAD aTDCf is achieved, whereas in the last row, combustion is delayed to an MFB50 of approximately 20 CAD aTDCf. Across all operating conditions, a strong agreement between experimental data and simulation results is observed. In the vast majority of cases, experimental and numerical traces of pressure and HRR are closely aligned. Only for the most delayed ST at $\lambda = 1.8$, the model slightly underpredict the combustion speed. Nevertheless, the simulation results remain well within the range of experimental variability. These results further confirm the predictive

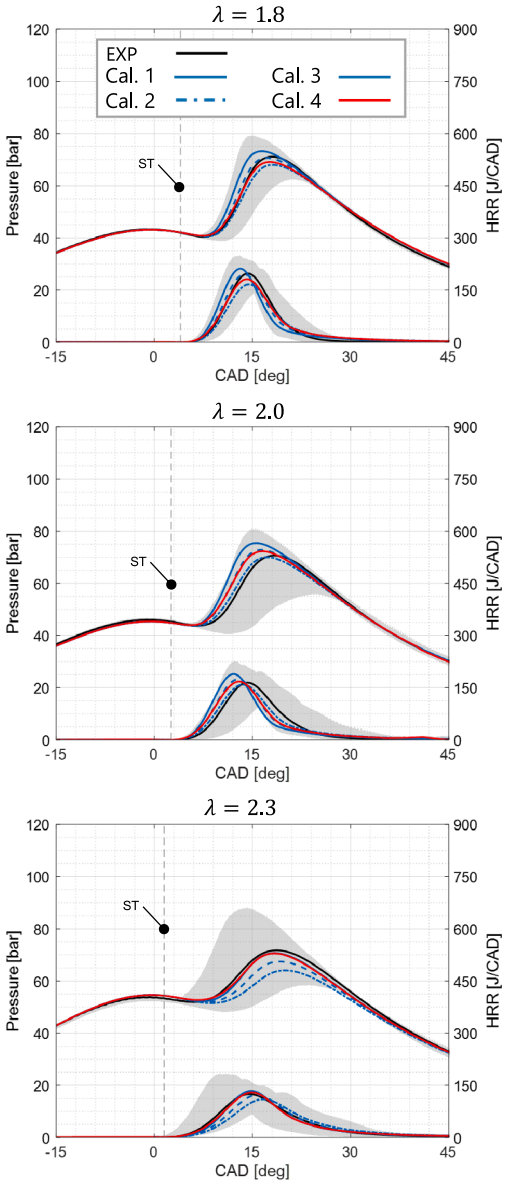

Fig. 3. Simulated and experimental pressure and heat release rate traces at $\lambda = 1.8$, $\lambda = 2.0$, and $\lambda = 2.3$.

capabilities of the developed model, which includes the effects of thermodiffusive instabilities.

4.3. Global effects of flame instabilities

As above mentioned, the impact of thermodiffusive flame instabilities on the combustion of lean hydrogen-air mixtures cannot be directly correlated with the global operating conditions. Rather, the influence of these instabilities on the relationship between laminar and freely propagating flame speeds is largely determined by the local λ encountered by the flame front at any given instant, along with the instantaneous pressure and temperature. Consequently, this section introduces a methodology that incorporates these variables to better interpret and explain the previously discussed findings. To assess the impact of thermodiffusive instabilities on the combustion process, three parameters of the flame front were selected and analyzed in the present work. These are:

- The mass-weighted average relative air-to-fuel ratio measured on the flame front (λ_{FF})
- The mass-weighted average instability parameter measured on the flame front (ω_{2FF})
- The mass-weighted relative difference between the freely propagating and the laminar flame speed measured on the flame front ($(S_M - S_L)/S_L$)

The flame front was identified through the mass progress variable $\widetilde{c}$ (where the tilde denotes a Favre average), which characterize the mixture breakdown between fresh and burned gases. Specifically, $\widetilde{c} = 0$ indicates the presence of only fresh gases, while $\widetilde{c} = 1$ signifies that only burned gases are present. In the present activity, all the cells of the computational domain featuring $0.1 < \widetilde{c} < 0.2$ were selected for the analysis in order to monitor the outer boundary of the flame, i.e., the one that directly interacts with the unburned gases. In *Fig. 5* the above-mentioned parameters are reported as a function of the in-cylinder mass fraction burned (x_b) for the three dilution levels analyzed, considering only the model which includes thermodiffusive instabilities (fourth row of Fig. 4). A threshold value of $\widetilde{c} = 0.1$ was adopted to distinguish between burned and unburned gases. In WP1 ($\lambda = 1.8$), λ_{FF} (Fig. 5a) purely depends on the local conditions of the mixture in the neighbourhoods of the spark plug at ST. Then, the flame intrinsically develops toward the richest volumes, which are characterized by higher flame speeds, and lastly the leanest portions of the mixture and consumed by the flame. Concurrently ω_{2FF} features a two-stage behaviour: initially, it remains almost constant with a value around 3, featuring a slight increment as combustion proceeds. Then, once x_b reaches 0.8, it rapidly increases up to 5 (Fig. 5c). This is mainly attributed to two concurrent phenomena. Firstly, as combustion progresses, a leaner mixture is encountered by the flame and in-cylinder pressure increases. Therefore, on the ω_2 maps reported in Fig. 6 for two different temperature levels, i.e. 900 K and 1000 K, that are representative of engine-like operations, combustion proceeds toward thermo-chemical conditions in which the impact of thermodiffusive flame instabilities on the mixture consumption rate is higher. However, at the same time, the temperature of the mixture entrained by the flame front slightly increases due to the heat transfer from the burned to the unburned gases. Hence, the ω_{2FF} increment is partially limited by this temperature increase. This aspect can be further clarified by comparing the ω_2 values obtained at 900 K and 1000 K and reported in Fig. 6. Indeed, while at 900 K the region characterized by nil ω_2 values (i.e., stable flame) is constrained to an extremely small area on the temperature-Φ map (low pressure and high Φ), at 1000 K the stable region expands up to $\lambda = 2.5$ ($\Phi = 0.4$) for low pressure levels (i.e., 10 bar) and up to 40 bar for almost stoichiometric mixtures (i.e., $\Phi = 0.8$). Moreover, the maximum ω_2 values reached on the diagonal ridge which splits the low-pressure region from the high-pressure region are almost doubled when reducing the temperature of the gases entrained by the flame from 1000 K to 900 K. The relative difference between S_M and S_L (Fig. 5d) increases following the same trend of ω_{2FF} and it is bounded between 15 % and 20 % until $x_b = 0.8$. Only towards the end of the combustion process (i.e., when $x_b > 0.8$) the relative difference between S_M and S_L increases, reaching values close to 50 %. These results are consistent with the $(S_M - S_L)/S_L$ maps shown in the right column of Fig. 6. As a matter of fact, until the combustion evolves close to the TDC, the temperature of the unburned gases remains around to 1000 K, and the relative difference between the freely propagating and the laminar flame speeds does not exceed 35 % across the entire pressure and Φ range. Specifically, at λ values near to 1.8 ($\Phi \approx 0.6$) and pressure levels between 40 and 80 bar, the relative difference between S_M and S_L is constrained between 15 % and 20 %. However, when lower temperatures of the unburned gases are considered (e.g. 900 K, which corresponds to the average temperature of the unburned gases during the expansion stroke in this operating condition) values up to 50 % are achieved on the $(S_M - S_L)/S_L$ map. In WP2

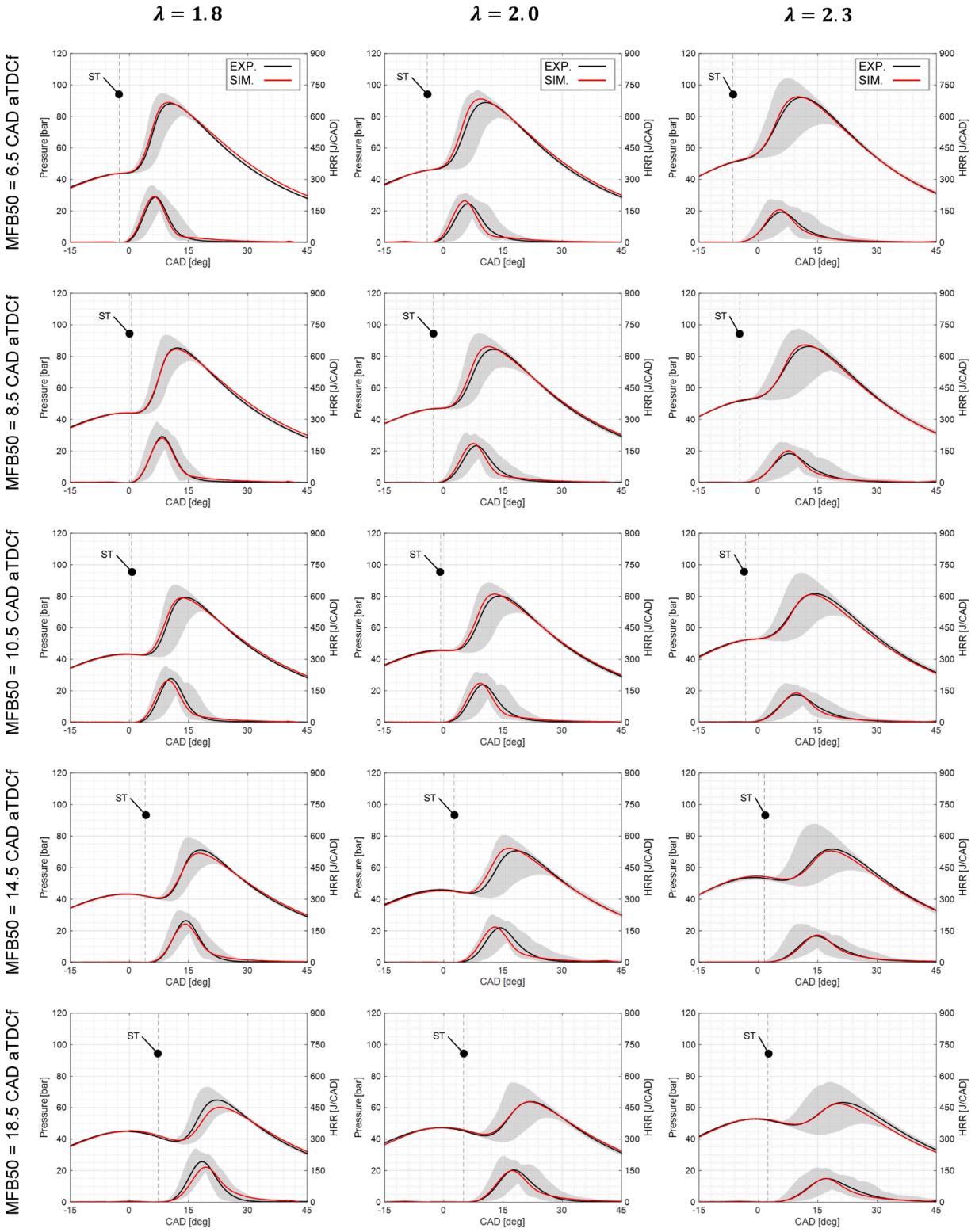

Fig. 4. Simulated and experimental pressure and heat release rate traces of a MFB50 sweep at $\lambda = 1.8$ (left column), $\lambda = 2.0$ (middle column), and $\lambda = 2.3$ (right column).

($\lambda = 2.0$), λ_{FF} follows roughly the same trend observed in WP1. λ_{FF} at ST is equal to the average operating relative air-to-fuel ratio. Successively the flame moves toward the richest volumes and lastly the leanest portions are entrained by the flame. In this operating condition, the average ω_2 of the flame front is higher compared to WP1 since the mixture consumed by the flame is leaner. Therefore, combustion evolves in areas of the ω_2 maps characterized by higher ω_2 values, thus increasing the importance of thermodiffusive instabilities. The relative difference between S_M and S_L is constrained between 20 % and 25 % from $x_b = 0$ up to $x_b = 0.8$. In WP3 the average dilution level of the mixture entrained by the flame is even higher. Consequently, ω_{2FF} increases and the relative difference between the freely propagating and the laminar flame

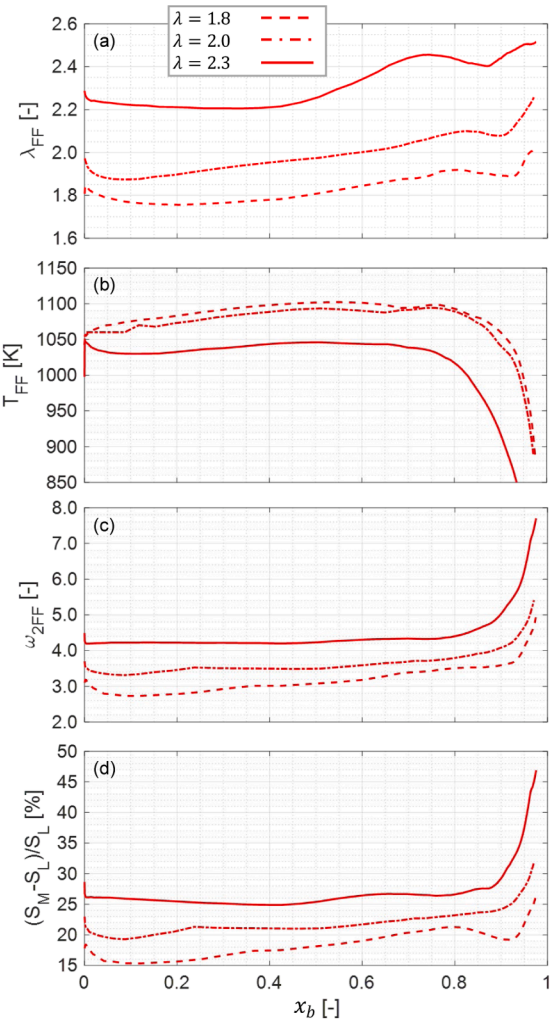

Fig. 5. λ_{FF} (a), T_{FF} (b) ω_{2FF} (c), and relative difference between the S_M and S_L (d) evaluated on the flame front identified through the progress variable $\tilde{c}$ ($0.1 < \tilde{c} < 0.2$).

speeds increases up to 25 %−30 %. For all the tested dilution levels, ω_{2FF} and $(S_M - S_L)/S_L$ significantly increase for $x_b > 0.8$ because of reduction of the unburned gases temperature occurring during the exhaust stroke.

The analysis of the progress of ω_2 for different dilution levels is crucial for interpreting combustion results reported in section 4.2. Indeed, the combustion model calibrated in WP3 and developed without correcting the tabulated flame speed maps with thermodiffusive flame instabilities (Cal. 3) displays a satisfactory agreement with experimental data solely for the calibration dilution level (i.e., $\lambda = 2.3$) and over-predicts combustion speed for the other two dilution levels. At the same time, the model calibrated in WP3 considering thermodiffusive instabilities (Cal. 4) features higher accuracy also for the other WPs. This because the implementation of thermodiffusive instabilities generates an unbalance in the flame speed maps used in the 3D-CFD model which enhances the propagation of the flame in lean environments and hinders its propagation in rich environments. Hence, even though the two models calibrated in WP3 with (Cal. 3) and without (Cal. 4) thermo-diffusive instabilities are identical in such operating condition, the consumption rate of the mixture at lower λ is well captured only by the model which includes flame instabilities. As a final remark, it is important to underline that ω_2 does not monotonically increases reducing Φ at a fixed pressure level, but it decreases if the mixture is particularly lean. For instance, the maximum ω_2 value is met for $\Phi = 0.35$ at a pressure equal to 40 bar and a temperature of 900 K (Fig. 6a). Then, a reduction in ω_2 is observed for lower Φ. As a result, the trends reported in Fig. 5b and c in terms of average ω_2 and average relative difference between S_M and S_L are solely valid for the WPs analyzed, and their extrapolation outside the validation domain might most likely lead to misleading results.

4.4. Local effects of flame instabilities

The implementation of thermodiffusive flame instabilities in the 3D-CFD combustion model generates also local modifications to the features of the flame, which are induced by the non-linear function that relates pressure, temperature, and Φ to ω_2. To assess them, three parameters have been defined and reported in Fig. 7 as a function of the mass fraction burned for the three dilution levels analyzed. They are:

- The equivalent radius of the semi sphere having the same volume of the burned gases (R_{Avg}). To define it, the cells of the computational domain with a value of the mass progress variable greater than 0.1 were assigned to the burned gases.
- The standard deviation of the distance between the spark plug and each point belonging to the flame front (R_{Std}) computed with respect to R_{Avg}. The same criterion adopted in section 4.3 was here adopted to define the flame front ($0.1 < \tilde{c} < 0.2$).
- The average air-to-fuel ratio of the burned gases (λ_b), where the burned gases are defined using the same criterion applied for determining R_{Avg}.

As expected, R_{Avg} is completely over imposed for the four different calibration procedures (Fig. 7a-c). Additionally, there is also a good agreement among the traces obtained for three tested dilution levels. This occurs because this parameter (R_{Avg}) is not affected by local features of the flame, but there exists a direct relation between the mass fraction burned and the volume swept by the flame. Instead, small but significant differences emerge between the model which account for thermodiffusive flame instabilities and those that neglect them, both in terms of R_{Std} and λ_b. Overall, the model that includes instabilities leads to slightly lower R_{Std} (Fig. 7d-f) compared to the other ones. The most relevant differences are obtained in the leanest WP since here the impact of flame instabilities is larger, as confirmed by the previous analysis. This means that, if thermodiffusive flame instabilities are implemented in the 3D-CFD combustion model, the flame tends to appear more spherical since the propagation of the flame is enhanced especially in the leanest portion of the flame front. This final consideration is supported by the plots reported in Fig. 7g-i. Indeed, from them appears evident that on average the mass entrained by the flame is leaner for the cases that consider flame instabilities, while it tends to consume richer mixtures if flame instabilities are neglected. As already observed for R_{Avg}, also for λ_b the largest differences are noticed for WP3 ($\lambda = 2.3$) since in this operating condition the higher values of ω_2 are reached. It is worth to point out thermodiffusive flame instabilities are not explicitly resolved in the simulation. Instead, their influence is indirectly captured through modified flame speed maps that account for such effects. As a result, the observed variations in R_{StD} and λ_b should be interpreted as mixture-driven manifestations of instability-sensitive flame propagation rather than direct evidence of resolved surface instabilities.

In Fig. 8 the relative difference between S_M and S_L assumed by all the points of the domain belonging to the flame front ($0.1 < \tilde{c} < 0.2$) are reported as a function of Φ and temperature for the three tested dilution rates. At 10 % mass fraction burned ($x_b = 0.10$) and $\lambda = 1.8$, this difference ranges from values close to zero (high-temperature – high-Φ) up to 30 % (low-temperature – low-Φ). Increasing the operating λ, as already shown in the previous analysis, the points shift toward the left part of the diagram and $(S_M - S_L)/S_L$ increases, up to values higher than 35 % at $\lambda = 2.3$. At $x_b = 0.50$, the number of points belonging to the flame front increases together with mixture stratification, as indicated

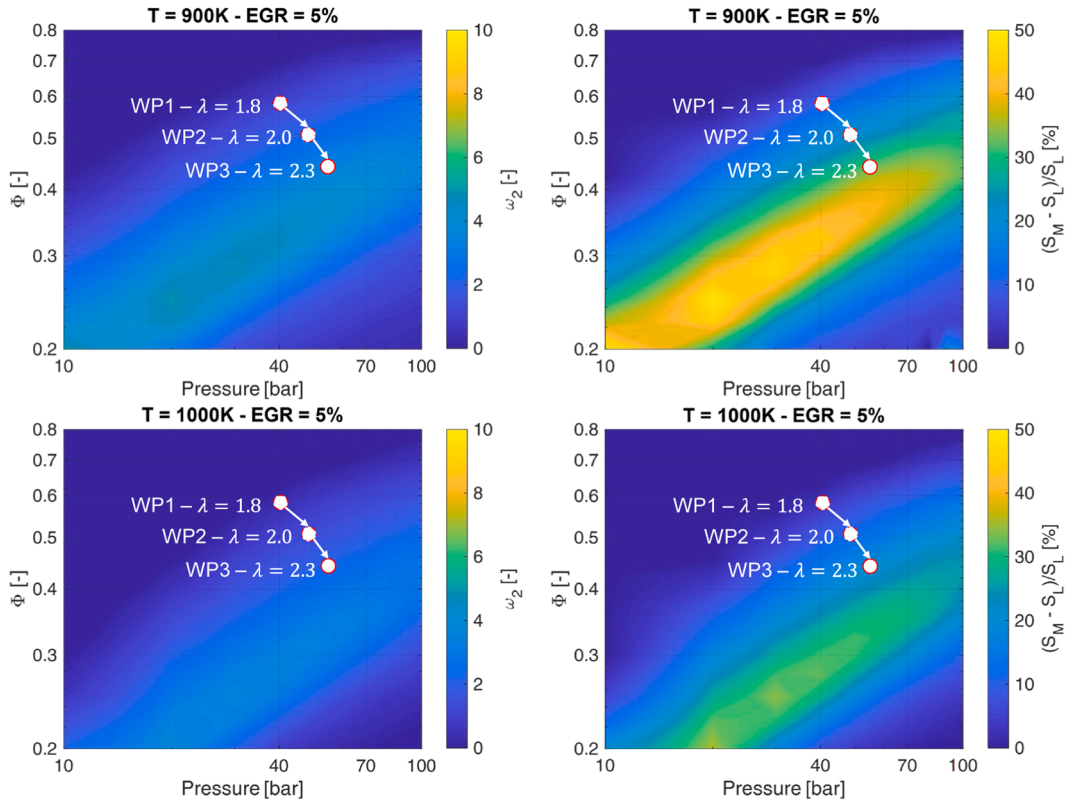

Fig. 6. Instability parameter ω_2 (left) and relative difference between freely propagating and laminar flame speed $(S_M - S_L)/S_L$ (right) at 900 K (a) and 1000 K (b) and EGR = 5 %, as a function of pressure and Φ.

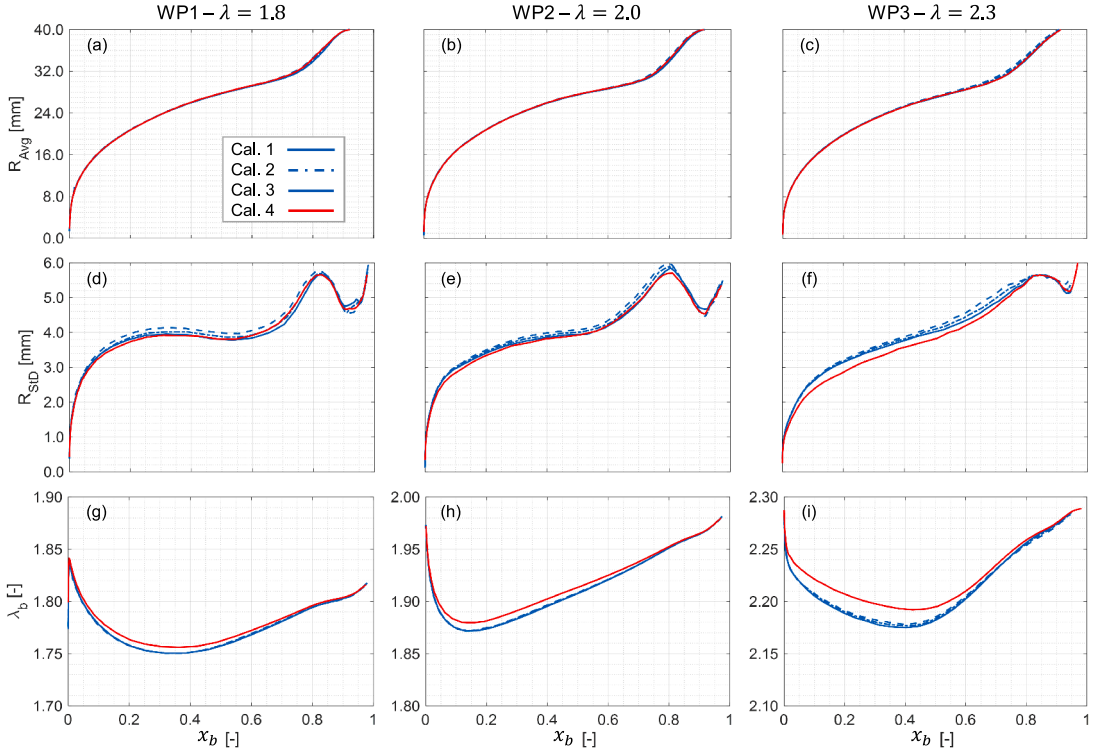

Fig. 7. Average flame radius (a-c), flame radius standard deviation (d-f), and average lambda of the burned mass (g-i), at $\lambda = 1.8$, $\lambda = 2.0$, and $\lambda = 2.3$.

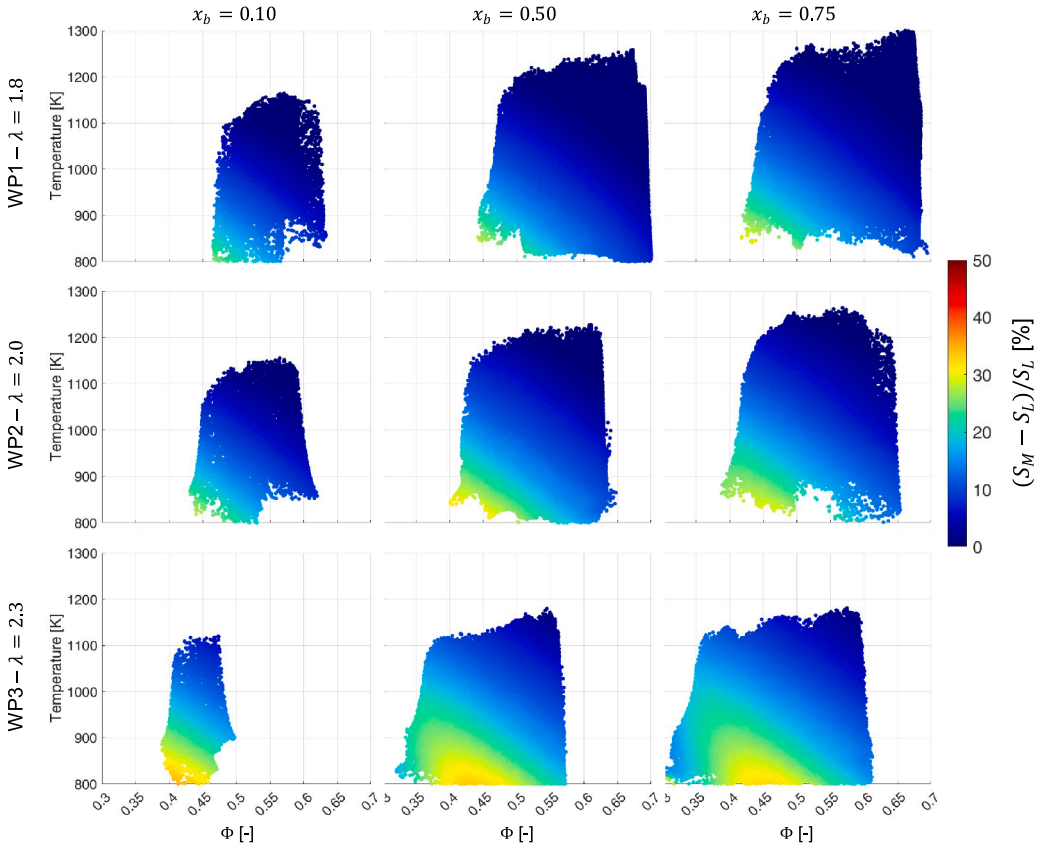

Fig. 8. Relative difference between S_M and S_L ($(S_M - S_L)\cdot 100/S_L$) as a function of Φ and temperature for $x_b = 0.10$, $x_b = 0.50$, and $x_b = 0.75$ at $\lambda = 1.8$, $\lambda = 2.0$, and $\lambda = 2.3$.

by the wider range of Φ that characterizes each operating point. Besides these small differences the same trends already seen at $x_b = 0.10$ remain valid, with higher $(S_M - S_L)/S_L$ values reached at $\lambda = 2.3$ in the low-temperature – low-Φ regions (up to 40 % for temperatures in between 850 and 900 K). Instead at $x_b = 0.75$, an interesting phenomenon is observed at $\lambda = 2.3$. Indeed, for extremely lean mixture (i.e., $\Phi < 0.35$), the relative difference between S_M and S_L is reduced, since the flame front develops in thermo-chemical conditions that on the ω_2 maps (reported in Fig. 6) lie below the diagonal ridge (i.e., high-pressure region). Additionally, this representation allows for a better explanation of the trends reported in Fig. 7, in terms of R_{StD} and λ_b. Indeed, at $\lambda = 1.8$, there is a wide area characterized by minimal or negligible differences between S_M and S_L. Hence, the trends of R_{Std} and λ_b is limited when comparing models that include thermodiffusive flame instabilities with those that do not. On the other hand, in the leanest working point, the relative difference between S_M and S_L reaches values as high as 45 % already for $x_b = 0.5$. As a result, the flame is driven to propagate towards leaner regions and to slow down in richer areas. This leads to a reduction of R_{StD} since the implementation of thermodiffusive flame instabilities counterbalance to some extent the stratification of the mixture.

5. Conclusions

In the present work, the impact of hydrogen thermodiffusive flame instabilities on the combustion process in a DI H2-ICE for off-road applications was assessed through 3D-CFD RANS simulations. Numerical simulations, relying on a flamelet-based combustion model (i.e., ECFM), were performed in a fixed working point (i.e., 1000 rpm – 200 Nm) under three dilution rates (i.e., $\lambda = 1.8$, $\lambda = 2.0$, and $\lambda = 2.3$). Two set of tabulated flame speed maps were derived: laminar flame speed (S_L) maps computed from 1D-CFD simulations in homogeneous reactor, and freely propagating flame speed (S_M) maps, based on the formulation proposed in [64] by Howarth and Aspden, which account for the effects of thermodiffusive instabilities through the evaluation of the instability parameter ω_2. This study provides further insight into the role of thermodiffusive instabilities when coupled with the ECFM model, offering a more in-depth analysis of the underlying physical mechanisms that govern their influence on combustion at both global and local scales. Simulations outcomes highlighted the need for including thermodiffusive flame instabilities in the numerical model in order to ensure model predictivity under a wider range of dilution rates. The main outcomes can be summarized as follows:

- The relevance of thermodiffusive instabilities on combustion is highly dependent on the operating conditions. Higher ω_2 values are obtained for leaner mixtures, enhancing the speed of flame propagation within the combustion chamber. At $\lambda = 1.8$, the average relative difference between S_M and S_L is bounded between 15 % and 20 %, while at $\lambda = 2.3$ it rises up to 30 %.
- When stratified mixtures are considered, the integration of thermodiffusive flame instabilities into 3D-CFD codes modifies the local features of the flame. This occurs because the magnitude of ω_2 is higher in the regions of the flame characterized by high dilution rates (low Φ), which also generally feature low temperatures. Nevertheless, if the mixture is excessively enleaned ($\Phi < 0.35$ in the WP at $\lambda = 2.3$), ω_2 decreases, reducing the relevance of thermodiffusive flame instabilities.
- Because of mixture stratification, which in turn generates an ω_2 stratification, the flame propagates slightly faster toward portions of the combustion chamber characterized by higher ω_2

values if thermodiffusive flame instabilities are included in the model.

The proposed methodology, which has so far been applied under operating conditions characterized by low *Ka* numbers ($Ka \leq 1$), lays the foundation for future developments aimed at defining a more comprehensive RANS numerical framework. Such a framework would be capable of accurately predicting and replicating the combustion process in SI H_2-ICEs, without being restricted to low *Ka* regimes, thereby extending its applicability to more turbulent conditions.

Although the model has been directly applied to engine-relevant conditions, a specific academic validation has not been specifically addressed and remains outside the scope of the present work.

CRediT authorship contribution statement

Andrea Scalambro: Writing – original draft, Visualization, Software, Investigation, Formal analysis, Conceptualization. **Andrea Piano:** Writing – review & editing, Supervision, Resources, Methodology, Conceptualization. **Federico Millo:** Writing – review & editing, Resources, Project administration.

Declaration of competing interest

The authors declare that they have no known competing financial interests or personal relationships that could have appeared to influence the work reported in this paper.

Acknowledgments

The Authors would like to acknowledge FEV Italia and Rehlko for providing the experimental data used in this study. Moreover, the Authors acknowledge the CINECA award under the ISCRA initiative, for the availability of high performance computing resources and support. Convergent Science provided CONVERGE licenses and technical support for this work.

References

[1] M. Yuan, J.Z. Thellufsen, H. Lund, Y. Liang, The electrification of transportation in energy transition, Energy 236 (2021), https://doi.org/10.1016/j.energy.2021.121564.
[2] World Energy Council, Global transport scenarios 2050, World Energy Council (2004). ISBN 9780946121144.
[3] F. Zhao, K. Chen, H. Hao, Z. Liu, Challenges, potential and opportunities for internal combustion engines in China, Sustainability (Switzerland) 12 (12) (2020), https://doi.org/10.3390/su12124955.
[4] H.R. Reitz, H. Ogawa, R. Payri, T. Fansler, IJER Editorial: the future of the internal combustion engine, Int. J. Engine Res. (2019), https://doi.org/10.1177/14680874198779.
[5] C. Tornatore, L. Marchitto, P. Sabia, M.De Joannon, Ammonia as green fuel in internal combustion engines: state-of-the-art and future perspectives, Front. Mech. Eng. 8 (2022), https://doi.org/10.3389/fmech.2022.944201.
[6] Kalghatgi Gautam, The outlook for fuels for internal combustion engines, Int. J. Engine Res. 15 (4) (2014) 383–398, https://doi.org/10.1177/1468087414526189.
[7] J. Martins, F.P. Brito, Alternative fuels for internal combustion engines, Energies (Basel) 13 (15) (2020), https://doi.org/10.3390/en13164086.
[8] A. Kowalewicz, Methanol as a fuel for spark ignition engines: a review and analysis, Proc. Inst. Mech. Engineers (1993) 43–52, https://doi.org/10.1243/PIME_PROC_1993_207_158_02.
[9] J. Vancoillie, J. Demuynck, L. Sileghem, M. Van De Ginste, S. Verhelst, L. Brabant, L. Van Hoorebeke, The potential of methanol as a fuel for flex-fuel and dedicated spark-ignition engines, Appl. Energy 102 (2013) 140–149, https://doi.org/10.1016/j.apenergy.2012.05.065.
[10] S. Verhelst, J.W. Turner, L. Sileghem, J. Vancoillie, Methanol as a fuel for internal combustion engines, Prog. Energy Combust. Sci. 70 (2019) 43–88, https://doi.org/10.1016/j.pecs.2018.10.001.
[11] C.P. Cooney, Yeliana, J.J. Worm, J.D. Naber, Combustion characterization in an internal combustion engine with ethanol - gasoline blended fuels varying compression ratios and ignition timing, Energy Fuels 23 (5) (2009) 2319–2324, https://doi.org/10.1021/ef800899r.
[12] Mendiburu Andrés, Lauermann Carlos, Hayashi Thamy, Marinos Diego, Berlini Rodrigues da Costa Roberto, Coronado Christian, Roberts Justo, Carvalho Joao de Jr., Ethanol as a renewable biofuel: combustion characteristics and application in engines, Energy 257 (2022), https://doi.org/10.1016/j.energy.2022.124688.
[13] A.K. Agarwal, Biofuels (alcohols and biodiesel) applications as fuels for internal combustion engines, Prog. Energy Combust. Sci. 33 (3) (2007) 233–271, https://doi.org/10.1016/j.pecs.2006.08.003.
[14] M. Mofijur, M.G. Rasul, J. Hyde, A.K. Azad, R. Mamat, M.M.K. Bhuiya, Role of biofuel and their binary (diesel-biodiesel) and ternary (ethanol-biodiesel-diesel) blends on internal combustion engines emission reduction, Renewable Sustainable Energy Rev. 53 (2016) 265–278, https://doi.org/10.1016/j.rser.2015.08.046.
[15] J. Hansson, S. Brynolf, E. Fridell, M. Lehtveer, The potential role of ammonia as marine fuel-based on energy systems modeling and multi-criteria decision analysis, Sustainability (Switzerland) 12 (8) (2020), https://doi.org/10.3390/SU12083265.
[16] J.S. Cardoso, V. Silva, R.C. Rocha, M.J. Hall, M. Costa, D. Eusébio, Ammonia as an energy vector: current and future prospects for low-carbon fuel applications in internal combustion engines, J. Clean. Prod. 296 (2021), https://doi.org/10.1016/j.jclepro.2021.126562.
[17] H. Xing, C. Stuart, S. Spence, H. Chen, Alternative fuel options for low carbon maritime transportation: pathways to 2050, J. Clean. Prod. 297 (2021), https://doi.org/10.1016/j.jclepro.2021.126651.
[18] C. Acar, I. Dincer, The potential role of hydrogen as a sustainable transportation fuel to combat global warming, Int. J. Hydrogen. Energy 45 (5) (2020) 3396–3406, https://doi.org/10.1016/j.ijhydene.2018.10.149.
[19] S. Verhelst, T. Wallner, Hydrogen-fueled internal combustion engines, Prog. Energy Combust. Sci. 35 (6) (2009) 490–527, https://doi.org/10.1016/j.pecs.2009.08.001.
[20] A. Onorati, R. Payri, B.M. Vaglieco, A.K. Agarwal, C. Bae, G. Bruneaux, M. Canakci, M. Gavaises, M. Günthner, C. Hasse, The role of hydrogen for future internal combustion engines, Editorial Int. J. Engine Res. (4) (2022) 529–540, https://doi.org/10.1177/14680874221081947ï.
[21] S. Verhelst, R. Sierens, S. Verstraeten, A critical review of experimental research on hydrogen fueled SI engines, SAE Trans (2006) 264–274, https://doi.org/10.4271/2006-01-0430.
[22] B.E. Milton, J.C. Keck, Laminar burning velocities in stoichiometric hydrogen and hydrogen-hydrocarbon gas mixtures, Combust. Flame 58 (1984) 13–22, https://doi.org/10.1016/0010-2180(84)90074-9.
[23] C.M. White, R.R. Steeper, A.E. Lutz, The hydrogen-fueled internal combustion engine: a technical review, Int. J. Hydrogen. Energy 31 (10) (2006) 1292–1305, https://doi.org/10.1016/j.ijhydene.2005.12.001.
[24] M. Faizal, L.S. Chuah, C. Lee, A. Hameed, J. Lee, M. Shankar, Review of hydrogen fuel for internal combustion engines, J. Mech. Eng. Res. Dev. 42 (3) (2019) 36–46, https://doi.org/10.26480/jmerd.03.2019.35.46.
[25] D.A. Crowl, Y.Do Jo, The hazards and risks of hydrogen, J. Loss. Prev. Process. Ind. 20 (2) (2007) 158–164, https://doi.org/10.1016/j.jlp.2007.02.002.
[26] Z. Stępień, A comprehensive overview of hydrogen-fueled internal combustion engines: achievements and future challenges, Energies (Basel) 14 (20) (2021), https://doi.org/10.3390/en14206504.
[27] Q.he Luo, B.gang Sun, Inducing factors and frequency of combustion knock in hydrogen internal combustion engines, Int. J. Hydrogen. Energy 41 (36) (2016) 16296–16305, https://doi.org/10.1016/j.ijhydene.2016.05.257.
[28] R. Ortiz-Imedio, A. Ortiz, I. Ortiz, Comprehensive analysis of the combustion of low carbon fuels (hydrogen, methane and coke oven gas) in a spark ignition engine through CFD modeling, Energy Convers. Manage 251 (2022), https://doi.org/10.1016/j.enconman.2021.114918.
[29] A. Piano, L. Rolando, S. Roggio, F. Millo, R. Tonelli, F. Gullino, F.S. Mortellaro, Experimental and numerical investigation of abnormal combustion phenomena in high-performance hydrogen direct-injection engine operated in stochiometric conditions, Int. J. Engine Res. (2024), https://doi.org/10.1177/14680874241302562.
[30] M.U. Manzoor, M.R. Yosri, M. Talei, F. Poursadegh, Y. Yang, M. Brear, Normal and knocking combustion of hydrogen: a numerical study, Fuel 344 (2023), https://doi.org/10.1016/j.fuel.2023.128093.
[31] Y. Ye, W. Gao, Y. Li, P. Zhang, X. Cao, Numerical study of the effect of injection timing on the knock combustion in a direct-injection hydrogen engine, Int. J. Hydrogen. Energy 45 (51) (2020) 27904–27919, https://doi.org/10.1016/j.ijhydene.2020.07.117.
[32] V. Dhyani, K.A. Subramanian, Fundamental characterization of backfire in a hydrogen fuelled spark ignition engine using CFD and experiments, Int. J. Hydrogen. Energy 44 (60) (2019) 32254–32270, https://doi.org/10.1016/j.ijhydene.2019.10.077.
[33] K.A. Subramanian, B.L. Salvi, A numerical simulation of analysis of backfiring phenomena in a hydrogen-fueled spark ignition engine, J. Eng. Gas. Turbine Power. 138 (10) (2016), https://doi.org/10.1115/1.4033182.
[34] L. Rouleau, F. Duffour, B. Walter, R. Kumar, L. Nowak, Experimental and Numerical Investigation On Hydrogen Internal Combustion Engine, SAE International, 2021, https://doi.org/10.4271/2021-24-0060. *SAE Technical Papers*.
[35] Z. Fu, W. Gao, Y. Li, X. Hua, J. Zou, Y. Li, Numerical simulation of the mixture distribution and its influence on the performance of a hydrogen direct injection engine under an ultra-lean mixture condition, Int. J. Hydrogen. Energy 48 (51) (2023) 19700–19712, https://doi.org/10.1016/j.ijhydene.2023.02.041.
[36] J. Gomez-Soriano, P. Sapkota, S. Wijeyakulasuriya, M. D'Elia, D. Probst, V. Viswanathan, M. Olcina-Girona, R. Novella, Numerical Modeling of Hydrogen Combustion Using Preferential Species Diffusion, Detailed Chemistry and Adaptive Mesh Refinement in Internal Combustion Engines, SAE International, 2023, https://doi.org/10.4271/2023-24-0062. *SAE Technical Papers*.

[37] B. Lee, H. Ge, S. Parameswaran, P. Zhao, CFD simulation of a premixed spark injection hydrogen engine, Proc. ASME (2019), https://doi.org/10.1115/ICEF2019-7257.

[38] T. Gammaidoni, A. Miliozzi, J. Zembi, M. Battistoni, Hydrogen mixing and combustion in an SI internal combustion engine: CFD evaluation of premixed and DI strategies, Case Stud. Thermal Eng. 55 (2024), https://doi.org/10.1016/j.csite.2024.104072.

[39] S. Sfriso, F. Berni, S. Breda, S. Fontanesi, C. Ramalho Leite, P. Brequigny, F. Foucher, Proposal and Validation of 3D-CFD Framework for Ultra-Lean Hydrogen Combustion in ICEs, SAE International, 2024, https://doi.org/10.4271/2024-01-2685. *SAE Technical Papers*.

[40] S. Verhelst, C. TJoen, J. Vancoillie, J. Demuynck, A correlation for the laminar burning velocity for use in hydrogen spark ignition engine simulation, Int. J. Hydrogen. Energy 36 (1) (2011) 957–974, https://doi.org/10.1016/j.ijhydene.2010.10.020.

[41] V.L. Zimont, Gas premixed combustion at high turbulence. Turbulent flame closure combustion model, Exp. Therm. Fluid. Sci. 21 (2000) 179–186.

[42] G. Maio, A. Boberic, L. Giarracca, D. Aubagnac-Karkar, O. Colin, F. Duffour, K. Deppenkemper, L. Virnich, S. Pischinger, Experimental and numerical investigation of a direct injection spark ignition hydrogen engine for heavy-duty applications, Int. J. Hydrogen. Energy 47 (67) (2022) 29069–29084, https://doi.org/10.1016/j.ijhydene.2022.06.184.

[43] F. Ramognino, L. Sforza, G. D'errico, J. Gomez-Soriano, A. Onorati, R. Novella, CFD Modelling of Hydrogen-Fueled SI Engines For Light-Duty Applications, SAE International, 2023, https://doi.org/10.4271/2023-24-0017. *SAE Technical Papers*.

[44] A. Kéromnès, W.K. Metcalfe, K.A. Heufer, N. Donohoe, A.K. Das, C.J. Sung, J. Herzler, C. Naumann, P. Griebel, O. Mathieu, M.C. Krejci, E.L. Petersen, W. J. Pitz, H.J. Curran, An experimental and detailed chemical kinetic modeling study of hydrogen and syngas mixture oxidation at elevated pressures, Combust. Flame 160 (6) (2013) 995–1011, https://doi.org/10.1016/j.combustflame.2013.01.001.

[45] V. Pessina, F. Berni, S. Fontanesi, A. Stagni, M. Mehl, Laminar flame speed correlations of ammonia/hydrogen mixtures at high pressure and temperature for combustion modeling applications, Int. J. Hydrogen. Energy 47 (61) (2022) 25780–25794, https://doi.org/10.1016/j.ijhydene.2022.06.007.

[46] L. Berger, A. Attili, H. Pitsch, Intrinsic instabilities in premixed hydrogen flames: parametric variation of pressure, equivalence ratio, and temperature. Part 2 – Non-linear regime and flame speed enhancement, Combust. Flame 240 (2022), https://doi.org/10.1016/j.combustflame.2021.111936.

[47] I. Hernandez, C. Turquand D'Auzay, R. Penning, E. Shapiro, J. Hughes, Thermo-Diffusive Flame Speed Adjustment and Its Application to Hydrogen Engines, SAE International, 2023, https://doi.org/10.4271/2023-01-0197. *SAE Technical Papers*.

[48] A.A. Konnov, Yet another kinetic mechanism for hydrogen combustion, Combust. Flame 203 (2019) 14–22, https://doi.org/10.1016/j.combustflame.2019.01.032.

[49] T.L. Howarth, A.J. Aspden, An empirical characteristic scaling model for freely-propagating lean premixed hydrogen flames, Combust. Flame 237 (2022), https://doi.org/10.1016/j.combustflame.2021.111805.

[50] L. Berger, A. Attili, H. Pitsch, Synergistic interactions of thermodiffusive instabilities and turbulence in lean hydrogen flames, Combust. Flame 244 (2022), https://doi.org/10.1016/j.combustflame.2022.112254.

[51] A.J. Aspden, M.S. Day, J.B. Bell, Characterization of low Lewis number flames, Proc. Combust. Inst. 33 (1) (2011) 1463–1471, https://doi.org/10.1016/j.proci.2010.05.090.

[52] S.K. Addepalli, Y. Pei, Y. Zhang, R. Scarcelli, Multi-dimensional modeling of mixture preparation in a direct injection engine fueled with gaseous hydrogen, Int. J. Hydrogen. Energy 47 (67) (2022) 29085–29101, https://doi.org/10.1016/j.ijhydene.2022.06.182.

[53] R. Scarcelli, T. Wallner, N. Matthias, V. Salazar, S. Kaiser, Numerical and optical evolution of gaseous jets in direct injection hydrogen engines, in: SAE 2011 World Congress and Exhibition, 2011, https://doi.org/10.4271/2011-01-0675.

[54] R. Scarcelli, T. Wallner, V.M. Salazar, S.A. Kaiser, Modeling and experiments on mixture formation in a hydrogen direct-injection research engine, SAe Int. J. Engines. (2009) 530–541, https://doi.org/10.4271/2009-24-0083.

[55] Amsden, A.A. and O'Rourke. P.J., "A particle numerical model for wall film dynamics in port-injected engines," *SAE Technical Papers*, 1996.

[56] A. Dhongde, P. Recker, H. Sankhla, L. Virnich, Advanced simulation methodologies for hydrogen combustion engines, in: 8th International Engine Conference - ATZ, 2021, https://doi.org/10.1007/s41321-021-0456-9.

[57] P.K. Senecal, E. Pomraning, M. Wang, Development of a species-based extended coherent flamelet model (SB-ECFM) for gasoline direct injection engine (GDI) simulations, in: Internal Combustion Engine Division Fall Technical Conference ICEF2018, 2018.

[58] V. Knop, A. Benkenida, S. Jay, O. Colin, Modelling of combustion and nitrogen oxide formation in hydrogen-fuelled internal combustion engines within a 3D CFD code, Int. J. Hydrogen. Energy 33 (19) (2008) 5083–5097, https://doi.org/10.1016/j.ijhydene.2008.06.027.

[59] O. Colin, A. Benkenida, C. Angelberger, 3D Modeling of mixing, ignition and combustion phenomena in highly stratified gasoline engines, Oil Gas Sci. Technol.-Rev. IFP 58 (1) (2003) 47–62.

[60] J.M. Duclos, D. Veynante, T. Poinsot, A comparison of flamelet LES models for premixed turbulent combustion, Combust. Flame 95 (1993) 101–117, https://doi.org/10.1016/0010-2180(93)90055-8.

[61] C. Meneveau, T. Poinsot, Stretching and quenching of flamelets in premixed turbulent combustion, Combust. Flame 86 (1991) 311–332, doi: 10.1016/0010-2180(91)90126-V.

[62] R. Blint, The relationship of the laminar flame width to flame speed, Combus. Sci. Technol. 49 (1–2) (1986) 79–92, https://doi.org/10.1080/00102208608923903.

[63] Y. Zhang, O. Mathieu, E.L. Petersen, G. Bourque, H.J. Curran, Assessing the predictions of a NOx kinetic mechanism on recent hydrogen and syngas experimental data, Combust. Flame 182 (2017) 122–141, https://doi.org/10.1016/j.combustflame.2017.03.019.

[64] T.L. Howarth, E.F. Hunt, A.J. Aspden, Thermodiffusively-unstable lean premixed hydrogen flames: phenomenology, empirical modelling, and thermal leading points, Combust. Flame 253 (2023), https://doi.org/10.1016/j.combustflame.2023.112811.

[65] F.A. Meziat Ramirez, Q. Douasbin, O. Dounia, O. Vermorel, T. Jaravel, Flame-turbulence interactions in lean hydrogen flames: implications for turbulent flame speed and fractal modelling, Combust. Flame 273 (2025), https://doi.org/10.1016/j.combustflame.2024.113926.

[66] M. Ilbas, A.P. Crayford, I. Yilmaz, P.J. Bowen, N. Syred, Laminar-burning velocities of hydrogen-air and hydrogen-methane-air mixtures: an experimental study, Int. J. Hydrogen. Energy 31 (12) (2006) 1768–1779, https://doi.org/10.1016/j.ijhydene.2005.12.007.

[67] M. Kuznetsov, S. Kobelt, J. Grune, T. Jordan, Flammability limits and laminar flame speed of hydrogen-air mixtures at sub-atmospheric pressures, Int. J. Hydrogen. Energy 37 (22) (2012) 17580–17588, https://doi.org/10.1016/j.ijhydene.2012.05.049.

[68] C.K. Law, C.J. Sung, Structure, aerodynamics, and geometry of premixed flamelets, Prog. Energy Combust. Sci. 26 (2000) 459–505.

[69] S. Verhelst, R. Woolley, M. Lawes, R. Sierens, Laminar and unstable burning velocities and Markstein lengths of hydrogen-air mixtures at engine-like conditions, Proc. Combust. Inst. 30 (1) (2005) 209–216, https://doi.org/10.1016/j.proci.2004.07.042.

[70] H. Pitsch, The transition to sustainable combustion: hydrogen- and carbon-based future fuels and methods for dealing with their challenges, Proc. Combust. Inst. 40 (1–4) (2024), https://doi.org/10.1016/j.proci.2024.105638.

[71] M. Matalon, C. Cui, J.K. Bechtold, Hydrodynamic theory of premixed flames: effects of stoichiometry, variable transport coefficients and arbitrary reaction orders, J. Fluid. Mech. 487 (2003) 179–210, https://doi.org/10.1017/S0022112003004683.

[72] H. Chu, L. Berger, T. Grenga, Z. Wu, H. Pitsch, Effects of differential diffusion on hydrogen flame kernel development under engine conditions, Proc. Combust. Inst. 39 (2) (2023) 2129–2138, https://doi.org/10.1016/j.proci.2022.07.042.

[73] X. Wen, L. Berger, L. Cai, A. Parente, H. Pitsch, Thermodiffusively unstable laminar hydrogen flame in a sufficiently large 3D computational domain – Part I: characteristic patterns, Combust. Flame 263 (2024), https://doi.org/10.1016/j.combustflame.2023.113278.

[74] L. Berger, M. Grinberg, B. Jürgens, P.E. Lapenna, F. Creta, A. Attili, H. Pitsch, Flame fingers and interactions of hydrodynamic and thermodiffusive instabilities in laminar lean hydrogen flames, Proc. Combust. Inst. 39 (2) (2023) 1525–1534, https://doi.org/10.1016/j.proci.2022.07.010.

[75] D. Bradley, M. Lawes, K. Liu, S. Verhelst, R. Woolley, Laminar burning velocities of lean hydrogen-air mixtures at pressures up to 1.0 MPa, Combust. Flame 149 (1–2) (2007) 162–172, https://doi.org/10.1016/j.combustflame.2006.12.002.

[76] M.S. Wu, S. Kwon, J.F. Driscoll, G.M. Faeth, Preferential diffusion effects on the surface structure of turbulent premixed hydrogen/air flames, Combus. Sci. Technol. 78 (1–3) (1991) 69–96, https://doi.org/10.1080/00102209108951741.

[77] C. Altantzis, C.E. Frouzakis, A.G. Tomboulides, M. Matalon, K. Boulouchos, Hydrodynamic and thermodiffusive instability effects on the evolution of laminar planar lean premixed hydrogen flames, J. Fluid. Mech. 700 (2012) 329–361, https://doi.org/10.1017/jfm.2012.136.

[78] X. Wen, T. Zirwes, A. Scholtissek, H. Böttler, F. Zhang, H. Bockhorn, C. Hasse, Flame structure analysis and composition space modeling of thermodiffusively unstable premixed hydrogen flames — Part II: elevated pressure, Combust. Flame 238 (2022), https://doi.org/10.1016/j.combustflame.2021.111808.

[79] X. Wen, T. Zirwes, A. Scholtissek, H. Böttler, F. Zhang, H. Bockhorn, C. Hasse, Flame structure analysis and composition space modeling of thermodiffusively unstable premixed hydrogen flames — Part I: atmospheric pressure, Combust. Flame 238 (2022), https://doi.org/10.1016/j.combustflame.2021.111815.

[80] L. Berger, A. Attili, H. Pitsch, Intrinsic instabilities in premixed hydrogen flames: parametric variation of pressure, equivalence ratio, and temperature. Part 1 - dispersion relations in the linear regime, Combust. Flame 240 (2022), https://doi.org/10.1016/j.combustflame.2021.111935.

[81] A.J. Aspden, M.S. Day, J.B. Bell, Turbulence-flame interactions in lean premixed hydrogen: transition to the distributed burning regime, J. Fluid. Mech. 680 (2011) 287–320, https://doi.org/10.1017/jfm.2011.164.

[82] Z. Liu, S. Yang, C.K. Law, A. Saha, Cellular instability in le < 1 turbulent expanding flames, Proc. Combust. Inst. 37 (2) (2019) 2611–2618, https://doi.org/10.1016/j.proci.2018.07.056.

[83] M. Matalon, The Darrieus-Landau instability of premixed flames, Fluid. Dyn. Res. 50 (5) (2018), https://doi.org/10.1088/1873-7005/aab510.

[84] L. Berger, A. Attili, H. Pitsch, Intrinsic instabilities in premixed hydrogen flames: parametric variation of pressure, equivalence ratio, and temperature. Part 2 – Non-linear regime and flame speed enhancement, Combust. Flame 240 (2022), https://doi.org/10.1016/j.combustflame.2021.111936.

[85] T.L. Howarth, A.J. Aspden, An empirical characteristic scaling model for freely-propagating lean premixed hydrogen flames, Combust. Flame 237 (2022), https://doi.org/10.1016/j.combustflame.2021.111805.